Introduction of a reverse simulation approach to identify the fatigue stress intensity factor crack arrest threshold from fretting cracking experiments

Alix De Pannemaecker, Siegfried Fouvry, Jean-Yves Buffiere

Introduction of a reverse simulation approach to identify the fatigue stress intensity factor crack arrest threshold from fretting cracking experiments

Alix de Pannemaecker[a,b,*], Siegfried Fouvry[a], Jean-Yves Buffière[b]

[a]LTDS, Ecole Centrale Lyon, 69134 Ecully, France

[b]MATEIS, INSA Lyon, 69100 Villeurbanne, France

The aim of this study was to estimate the ΔK_{th} crack arrest stress intensity factor related to the crack arrest condition of a material subjected to partial slip fretting loadings, by coupled experimental and numerical simulation. The study focuses on a plane (Al-alloy)/cylinder (TA6V) interface. Fretting tests were performed for each configuration to obtain the crack length as a function of the number of fretting cycles, in order to establish the crack length related to crack arrest condition. Using a reverse FEM analysis of crack arrest fretting experiments, the thresholds $\Delta K_{th(fr)}$ are extracted. Two 2196-T8 and 2196-UA aluminium alloys were compared, while the short crack arrest versus the crack length evolutions were formalized using a Kitagawa Takahashi formalism.

1. Introduction

Araujo et al. [1] demonstrated that fretting fatigue endurance can be formalized using a short crack arrest methodology. This approach was adopted in [2] to estimate the crack arrest boundary in the fretting fatigue map approach. Such analysis consists in computing the evolution of the stress intensity factor as a function of crack length and assessing whether this *K*-factor loading path intercepts the short crack arrest boundary. If the ΔK_{eff} loading path crosses the boundary, then fretting fatigue failure can be expected. Note that the short crack arrest boundary [3] is approximated using either the Kitagawa Takahashi or the El-Haddad formalism [2].

This methodology usually considers a crack located at the contact border, perpendicular to the contact surface. However, experimental results show that the crack path below the interface is more complex and usually displays in the first stages of growth an oblique angle oriented towards the inner part of the contact. A major question is whether the normal crack approximation is able to describe real crack path evolution.

A second aspect concerns the short crack methodology which is usually applied to approximate the crack arrest condition. The present study considered an original reverse approach, consisting in estimating the $\Delta K_{th(fr)}$ (threshold crack arrest intensity factor) in partial slip fretting for the studied material, by applying a reverse identification method to the experimental plain fretting cracking results. The study focused on cylinder/plane fretting models with TA6V/Al-alloys (2196-T8 and 2196-UA) under partial slip conditions.

2. Materials and experimental procedure

2.1. Materials

A 2196 aluminium alloy was investigated, with a chemical composition detailed in Table 1.

Two different heat treatments were investigated: industrial peak aged, called T8, and an experimental treatment at low temperature (120 °C for 96 h), called Under-Aged (UA). These two ageing treatments involve equivalent elastic properties with an elastic modulus *E* of about 79,000 MPa and a Poisson's coefficient about 0.305, but with differing monotonic and cyclic mechanical properties such as ultimate stress R_m, yield stress $R_{0.2}$, elongation rate *A%* and fatigue limit σ_d (Table 2). The related ΔK_0 long crack arrest thresholds are unfortunately not available. However, according to the differences in fatigue limits and R_m values, different ΔK_0 values can be expected, such that $\Delta K_{0(UA)} > \Delta K_{0(T8)}$.

* Corresponding author at: LTDS, Ecole Centrale Lyon, 36 avenue Guy de Collongue, 69134 Écully CEDEX, France.
Tel.: +33 4 78 18 60 44
E-mail address: alix.de-pannemaecker@ec-lyon.fr (A. de Pannemaecker).

Nomenclature

Material properties

E	Young's modulus
ν	Poisson's coefficient
R_m	ultimate stress
$R_{0.2}$	yield stress
$A\%$	elongation rate
σ_d	fatigue limit
ΔK_0	nominal threshold stress intensity factor range value related to the long crack arrest condition (constant value)
$\Delta K_{0(fr)}$	range of the fretting long crack arrest stress intensity factor threshold

Contact loadings, stress and crack parameters

P	linear normal force
Q	fretting linear tangential force
Q^*	fretting linear tangential force amplitude
δ	fretting displacement
δ^*	fretting displacement amplitude
$R_{(fr)}$	fretting stress ratio (Q_{min}/Q_{max})
R	radius of the cylinder pad
W	width of the specimen
N	number of cycles
$p_{max}=p_0$	Hertzian maximum peak pressure
q_{max}	maximum interfacial shear stress at $x=-c$
μ	coefficient of friction
μ_t	coefficient of friction at the sliding transition
μ_{crack}	coefficient of friction in the crack
a	half width of the contact area
c	radius of the stick zone
b	crack length
b_p	maximum projected crack length (to the normal of the surface)
b_{p_CA}	maximum projected crack length related to the crack arrest condition
b_0	short crack/long crack transition
$b_{0(fr)}$	fretting short crack/long crack transition
σ_{11max}	maximum principle stress
σ_{11}	principle stress
J	strain energy release rate
ΔK_{th}	crack arrest stress intensity factor threshold
ΔK_{eff}	effective stress intensity factor range
K_I	mode I stress intensity factor
K_{II}	mode II stress intensity factor
K_{Imax}	mode I stress intensity factor at $+Q$
K_{Imin}	mode I stress intensity factor at $-Q$
K_{IImax}	mode II stress intensity factor at $+Q$
K_{IImin}	mode II stress intensity factor at $-Q$
ΔK_I	nominal stress intensity factor in mode I ($K_{Imax}-K_{Imin}$)
ΔK_{II}	nominal stress intensity factor in mode II ($K_{IImax}-K_{IImin}$)

Subscripts

GS	gross slip
PS	partial slip
avg	average value
_KINKED	kinked crack path
_NORMAL	normal crack path
_I	mode I
_II	mode II
_CA	crack arrest condition
(K–T)	related to the Kitagawa Takahashi approximation
(C-T)	related to C-T experiments
(fr)	value extrapolated from the reverse fretting crack arrest analysis
(UA)	related to 2196-UA
(T8)	related to 2196-T8

For each alloy, small cubic specimens were machined and polished to achieve a 0.2 μm R_a roughness. Samples were adjusted so that fretting loading was applied in the rolling direction of the alloy (Fig. 1).

2.2. Plain fretting experiment

Plain partial slip fretting tests were performed using a hydraulic set-up at the LTDS laboratory, as previously described by Heredia [5]. The normal force (P) was kept constant while tangential force (Q) and displacement (δ) amplitudes were recorded. The fretting loop could be plotted and the corresponding amplitude values (respectively Q^* and δ^*) defined (Fig. 2). The stress ratio was kept at $R_{(fr)}=-1$.

In the present fretting cracking investigation, the displacement amplitude was monitored in order to maintain partial slip conditions, keeping tangential force amplitude constant throughout the test. A cylinder/plane configuration was applied. The fretting pad consisted of a Ti–6Al–4V alloy, displaying the following elastic properties: 119,500 MPa elastic modulus and 0.287 Poisson coefficient. Two cylinder radius configurations were investigated: $R=40$ mm and $R=80$ mm. The maximum constant Hertzian pressure was fixed at $p_{max}=300$ MPa, adjusting linear normal force to $P=217$ N/mm and $P=436$ N/mm respectively. The lateral width of the cylinder pad was about 8 mm, allowing plane strain conditions to be assumed along the median axis of the fretting scar. Preliminary tests determined the friction coefficient at the sliding transition $\mu_t=0.85$ [4]. Note that no fatigue test was performed: only contact loads were applied so that,

Table 2
Mechanical properties of the 2196 aluminium, according to heat treatment.

State	$R_{0.2}$ (MPa)	R_m (MPa)	A (%)	σ_d (MPa) at 10^7 cycles
T8	559	594	5.9	150
UA	428	520	11.1	140

Table 1
Chemical composition of the 2196 aluminium.

% Cu	% Li	% Mg	% Mn	% Ag	% Zr	% Zn	% Si	% Fe
2.5–3.3	1.4–2.1	0.25–0.8	< 0.35	0.25–0.6	0.04–0.18	< 0.35	< 1.2	< 0.15

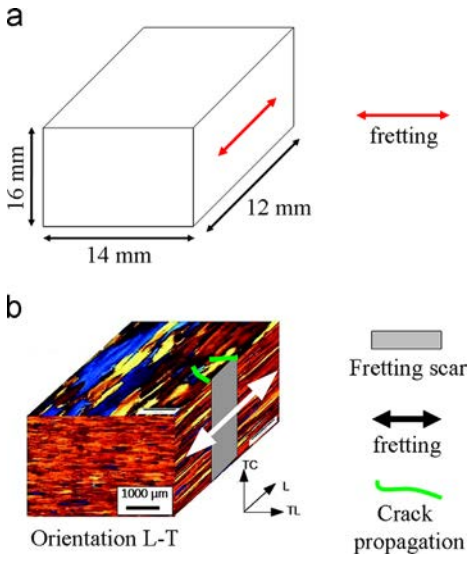

Fig. 1. Fretting sample (a) Sample geometry and (b) microstructure [4].

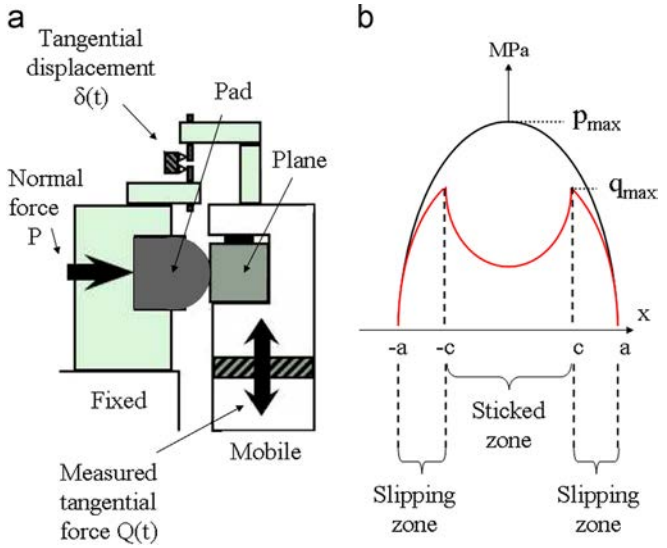

Fig. 2. Fretting tests (a) experimental set-up [2,5] and (b) pressure and shear distributions applied on the plane at $+Q^*$.

wherever the applied fretting stressing, a crack arrest condition would be systematically achieved.

Fig. 2b illustrates shear and pressure distributions applied at the surface of the aluminium sample. The macroscopic tangential load $\pm Q^*$ leading the cylinder generates a maximal shear q_{max} on the plane. This value determines the stress level generated in simple fretting: $\sigma_{11\ max} = 2q_{max}$ at $R_{(fr)} = -1$ [6]. For this reason, the variable q_{max} was used to calibrate and compare all experimental situations.

3. Experimental results

The following destructive method was applied: after each fretting test of N number of cycles, the plane sample was cut along the median axis of the fretting scar [15]. Observations on the cross section were performed to measure the fretting crack length. The objective was to identify the evolution of crack length as a function of fretting cycle, so as to establish a "plateau" value related to the crack arrest condition. The tangential force was kept constant throughout the experiment, with $q_{max} = 190$ MPa at $+Q^*$. This tangential loading had been previously adjusted to guarantee significant fretting cracking for elastic configurations (i.e., Von Mises equivalent stress less than $R_{0.2}$).

Fig. 3 shows a typical crack path observed for the studied configuration after 2×10^6 cycles. As usually observed, the incipient crack propagation approximates a 45° orientation compared to the normal plane of the surface until about 30 µm in depth. Below 200 µm, the crack propagation direction is normal to the plane. Between 30 and 200 µm, the crack path is considered linear, with a 10° angle with respect to the normal of the surface. A schematic description of the crack path is given in Fig. 3. Most of the crack analysis showed similar evolution, so that the overall crack path could be described by linear segments (Fig. 3); taking the average, the first angle was kept at 47.5°, the second at 15.5 and the last at 0° for the numerical model presented below.

This typical crack path evolution will be considered later for crack modelling. To simplify crack length analysis, only the projected crack length (b_p parameter in Fig. 3) was considered. Fig. 4 compares the evolution of maximum projected crack length b_p as a function of the number of fretting cycles.

For both materials, asymptotic evolutions can be observed. This analysis shows that the maximum crack length stabilized after 10^6 cycles. Considering the asymptotic value obtained after 2×10^6 cycles, the maximum crack lengths (b_{p_CA}) related to the crack arrest condition can now be estimated for the studied plain fretting condition ($R = 80$ mm, $p_{max} = 300$ MPa, $q_{max} = 190$ MPa

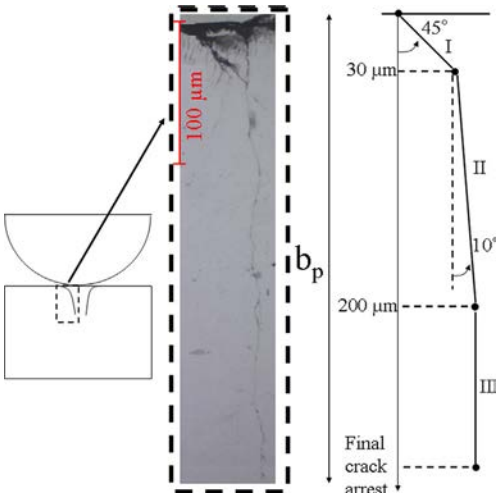

Fig. 3. Diagram and photo of the real crack path description – 2196-T8 at $N = 2 \times 10^6$, $R = 80$ mm, $q_{max} = 190$ MPa.

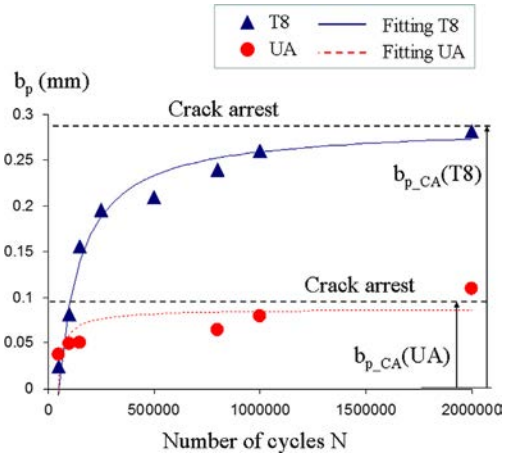

Fig. 4. Propagation curves, $R = 80$ mm, $q_{max} = 190$ MPa.

Table 3
Test conditions and related analysis of crack arrest conditions.

	UA					T8					
R (mm)	40	40	80	80	80	40	40	40	80	80	80
P (N/mm)	217	217	436.5	436.5	436.5	217	217	217	436.5	436.5	436.5
Q (N/mm)	99.5	124.5	150	200	250	76	99.5	124.5	150	200	250
a (mm)	0.46	0.46	0.92	0.92	0.92	0.46	0.46	0.46	0.92	0.92	0.92
p_{max} (MPa)	300	300	300	300	300	300	300	300	300	300	300
q_{max} (MPa)	190	210	160	190	210	160	190	210	160	190	210
μ	0.85	0.85	0.85	0.85	0.85	0.85	0.85	0.85	0.85	0.85	0.85
μ_{crack}	0.57	0.57	0.57	0.57	0.57	0.57	0.57	0.57	0.57	0.57	0.57
b_{p_CA} (mm)	0.027	0.069	0.032	0.11	0.17	0.033	0.071	0.130	0.089	0.282	0.45
b_{p_CA}/a	0.059	0.150	0.035	0.120	0.185	0.072	0.154	0.283	0.097	0.307	0.489
K_{Imax} (MPa m$^{0.5}$)	0.6	1.5	2	2.5	3.2	1.4	1.6	1.7	1.8	1.4	1.7
K_{Imin} (MPa m$^{0.5}$)	−2.6	−2.4	−3.5	−1.7	−1.4	−2.8	−2.3	−1.5	−1.9	−1.1	−0.6
K_{IImax} (MPa m$^{0.5}$)	1.1	0.7	0.7	0.8	1.1	0.4	0.6	0.9	0.4	0.8	0.8
K_{IImin} (MPa m$^{0.5}$)	−0.9	0.6	0	0.6	0.9	−0.1	0.4	0.9	0.1	1.3	1.4
ΔK_{IImin} (MPa m$^{0.5}$)	2	0.2	0.7	0.2	0.2	0.4–0.1	0.2	0	0.2	0.5	0.6
R (K_{Imin}/K_{Imax})	−4.1	−1.6	−1.7	−0.7	−0.4	−2	−1.5	−0.9	−1	−0.7	−0.4
ΔK_{eff} (MPa m$^{0.5}$)	2.1	1.5	2.2	2.5	3.3	1.5	1.6	1.7	1.8	1.5	1.8

at $+Q^*$). For the T8 and UA ageing treatments respectively, $b_{p\_CA}(T8)=280$ μm and $b_{p\_CA}(UA)=100$ μm. The maximum crack length achieved for T8-ageing was longer than for UA-ageing: i.e., heat treatment UA enabled better material resistance to crack propagation. It can be intuited that the threshold Stress Intensity Factor related to the T8-treatment was significantly smaller than that expected for UA-ageing. The following analysis quantifies this aspect.

Assuming that crack arrest conditions are achieved after 2×10^6 cycles, the analysis was extended, keeping maximum pressure $p_{max}=300$ MPa constant and investigating two maximum interfacial shear loads, $q_{max}=160$ MPa and $q_{max}=210$ MPa, using two different cylinder radii, $R=40$ mm and $R=80$ mm. The obtained maximum crack lengths are compiled in Table 3. This analysis confirmed the previous conclusions: the b_{p_CA} values obtained for the T8 heat treatment were systematically longer than these obtained for the UA treatment. This confirms that the UA heat treatment improved the crack propagation resistance.

Indeed, the morphology of the crack path related with the UA treatment was much more disturbed than with T8 (Fig. 5). This suggests that a larger driving force was required to propagate the crack, which indirectly explains the shorter crack lengths related to the 2196-UA crack arrest conditions.

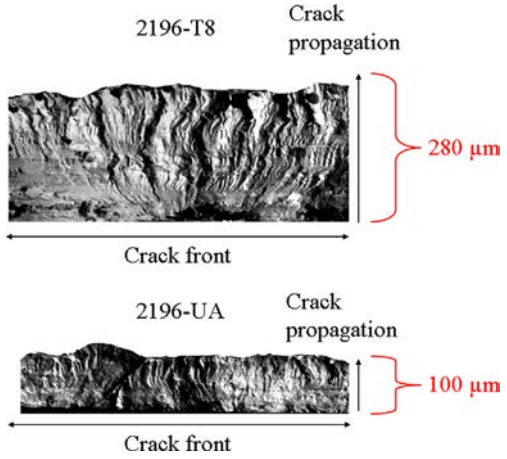

Fig. 5. 2196-T8 and 2196-UA, crack profiles for $q_{max}=190$ MPa and $R=80$ mm at $N=2\times10^6$ cycles.

4. FEM computation of Stress Intensity Factor evolution below the fretting contact

4.1. Contact modelling

All the FEM models (Abaqus 6.9) presented in this paper were automatically generated by a code developed in the LTDS laboratory (automatic remeshing of the crack tip coupled with Matlab).

Two equivalent 2D-plane strain FEM models were constructed to simulate the studied $R=40$ mm and $R=80$ mm plain fretting tests. All the elastic and friction properties previously determined during the experimental tests were implemented in the FEM models. The fretting model was composed of a fixed plane and a moving cylindrical pad (Fig. 6a). The mesh was composed of triangular (CPE3) and quadratic (CPE4R) linear elements. Quadratic elements were used to define the crack tip zone in a round domain of 5-μm radius. Outside the crack tip zone, triangular elements were considered, in order to reduce time costs. The mesh size in the contact zone was refined down to 20 μm in order to provide a more accurate estimate of the contact stress fields. The contact and the crack were described by a master-slave

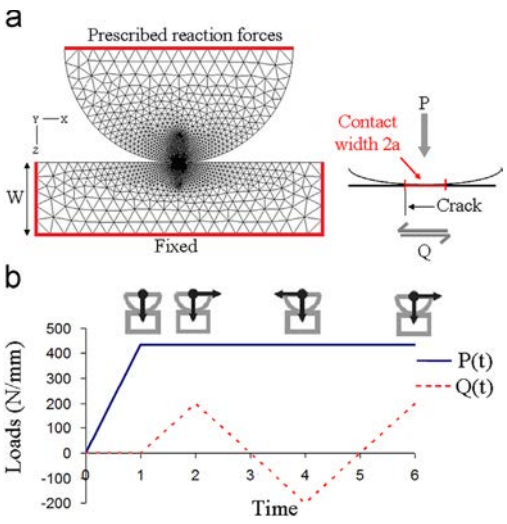

Fig. 6. FEM description of the plain fretting cracking experiments [14] ($R=80$ mm, $p_{max}=300$ MPa, $P=436$ N/mm and $q_{max}=190$ MPa at $Q^*=200$ N/mm) (a) FEM model and (b) loads applied.

algorithm, and the tangential loading was determined by Lagrange multipliers with a constant friction coefficient ($\mu_t=0.85$). This value was determined on a variable displacement test. For

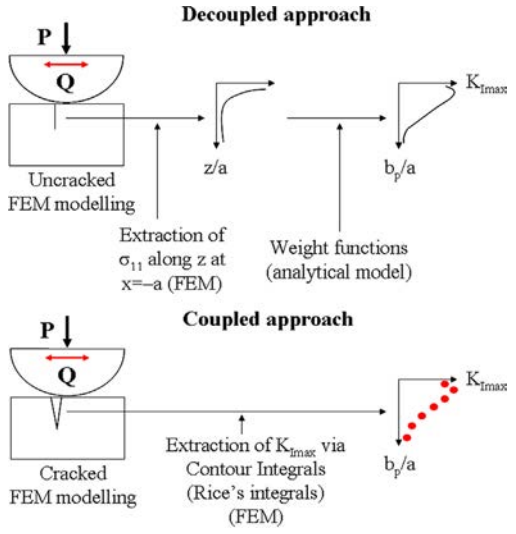

Fig. 7. Illustration of the decoupled and coupled approaches applied to estimate the mode I stress intensity factor.

each cylinder/plane model, both linear normal force and cyclic alternated tangential forces were adjusted to achieve the required p_{max} and q_{max} interfacial stressing loading (Fig. 6).

As elastic loads were imposed, cracking computation was restricted to a single loading cycle. Results and interpretations were made for a single crack located at the trailing contact border ($x=-a$) at the loading stage ($Q=Q^*$ at $t=6$), which implies an open crack condition, and also at ($Q=-Q^*$ at $t=4$) which implies a closed crack condition (Fig. 6).

Two different approaches to estimate of the Stress Intensity Factor were addressed (Fig. 7):

(a) *Decoupled Approach*, which consists in modelling an uncracked FEM Cylinder/Plane model, and then extracting the stress field along the z axis at the contact border to finally apply the common weight functions [7], so as to estimate the stress intensity factors and
(b) *Coupled Approach*, which consists in modelling a cracked FEM Cylinder/Plane model at the contact border and applying the Contour Integrals method extracted from the Rice's Integrals [8], which finally enables the stress intensity factors to be established.

For a two-dimensional model, the strain energy release rate J defined from the Rice's integral is expressed by:

$$J=\int_{\Gamma}\left(W\,dx_2-t\frac{\partial u}{\partial x_1}ds\right) \tag{1}$$

where $W(x_1,x_2)$ is the strain energy density, $t=n\sigma$ is the surface traction vector, n is the normal to the curve Γ, σ is the Cauchy stress tensor and u is the displacement vector.

The strain energy density is given by:

$$W=\int_0^{\varepsilon}\sigma\,d\varepsilon \quad \text{with } \varepsilon=\tfrac{1}{2}[\nabla u+(\nabla u)^T] \tag{2}$$

For a plane strain mixed-mode model, the J-integral is also related to stress intensity factors by the following equation:

$$J=K_{\mathrm{I}}^2\left(\frac{1-\nu^2}{E}\right)+K_{\mathrm{II}}^2\left(\frac{1-\nu^2}{E}\right) \tag{3}$$

The energy release rate is easily calculated by Abaqus but stress intensity factors are not so directly computed from a known J-integral for mixed-mode problems. The software provides an interaction integral method to extract stress intensity factors [9–11]. Two states of the cracked body are considered: state 1 $(\sigma_{ij}^{(1)},\varepsilon_{ij}^{(1)},u_i^{(1)})$ related to the present state, and state 2 $(\sigma_{ij}^{(2)},\varepsilon_{ij}^{(2)},u_i^{(2)})$, defined as an auxiliary state corresponding to asymptotic fields for mode I or mode II. The J-integral for the two states leads to Eq. (4), with $I^{(1,2)}$ the interaction integral for states 1 and state 2:

$$J^{(1+2)}=J^{(1)}+J^{(2)}+I^{(1,2)} \tag{4}$$

Eq. (3) leads to:

$$J^{(1+2)}=J^{(1)}+J^{(2)}+\frac{2(1-\nu^2)}{E}(K_I^{(1)}K_I^{(2)}+K_{II}^{(1)}K_{II}^{(2)}) \tag{5}$$

From (4) and (5) we have:

$$I^{(1,2)}=\frac{2(1-\nu^2)}{E}(K_I^{(1)}K_I^{(2)}+K_{II}^{(1)}K_{II}^{(2)}) \tag{6}$$

Mode I can now be extracted by choosing state 2 as the pure asymptotic fields with $K_{\mathrm{I}}^{(2)}=1$ and $K_{\mathrm{II}}^{(2)}=0$, which finally leads to:

$$K_I^{(1)}=\frac{2(1-\nu^2)}{E}I^{(1,\ \mathrm{model})} \tag{7}$$

The mode II stress intensity factor is extracted using a similar strategy.

The coupled approach is theoretically the more consistent given that it considers the presence of the crack, for the contact stress analysis. However, it is time-consuming and fastidious as, for each crack length, dedicated meshing and FEM simulations are required. The decoupled strategy is therefore usually preferred. Only a single FEM simulation of an uncracked interface is required to extract the stress field: the evolution of the stress intensity factor values as a function of crack length is extracted from an adequate application of the weight function approach developed from Bueckner's formalism [7].

Besides, a critical aspect of the coupled approach relates to mesh refinement at the crack tip, which can influence stress intensity factor estimations. To optimise this aspect, a simple normal crack inserted in an aluminium plain fatigue specimen was simulated and compared with established weight function result computations. A very good correlation was achieved if the mesh refinement at the crack tip was about 0.5 μm (Fig. 8). This critical mesh size was systematically applied in all the fretting cracking simulations. Note that the equivalence of the contour integral and weight function approaches is only valid in this

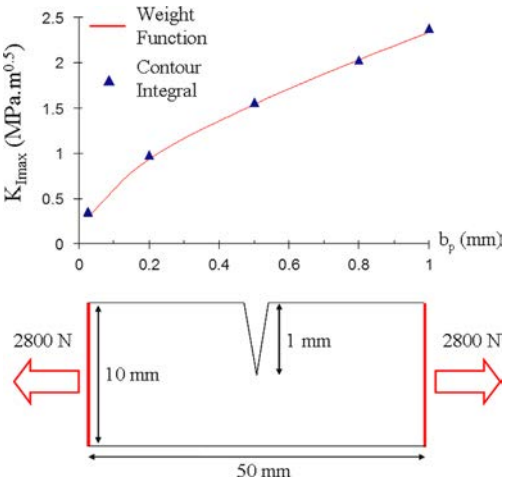

Fig. 8. Equivalence of the decoupled and coupled approaches on a single edge crack in an aluminium sample in tension.

particular case. Indeed, it depends on the geometry, boundary conditions and availability of weight functions.

4.2. Comparison of the decoupled and coupled approaches for K_{Imax} estimation

The decoupled and coupled approaches were compared to establish which was the more appropriate for describing the fretting cracking process. This analysis was restricted to mode I evolution of a normal crack located at the trailing contact border. Note that this simplified description is the one usually adopted in the literature [2].

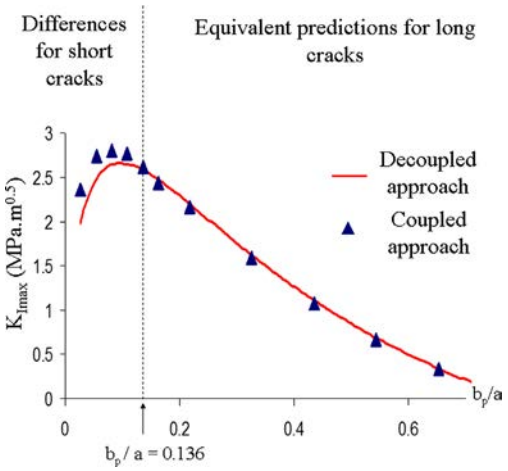

Fig. 9. K_{Imax} estimations by the decoupled and coupled approaches; q_{max} = 190 MPa, R = 80 mm.

Fig. 9 shows the evolution of K_{Imax} as a function of the crack length. It reveals that both methods are equivalent for long cracks ($b_p/a > 0.136$), leading to superposed evolutions. But differences are observed for shorter cracks, the coupled method leading to larger K_{Imax} values. This difference for short cracks is directly bound to the shear and pressure distributions (Fig. 10).

As expected, the uncoupled model is related to a perfect Hertzian profile (Fig. 10a), as the presence of a crack is not considered for the contact stress analysis. In contrast, the coupled approach shows a pressure peak and shear discontinuities at the contact border ($x = -a$). The presence of the crack leads to local overstressing, which increases the K_{Imax} value in the region near the surface (Fig. 10b). When the crack gets longer, the crack tip moves away from the surface, so that the effect of these very local pressure and shear discontinuities decreases. Similar conclusions were previously made by Giner et al. [12]. The limit of this effect is identified for $b_p = 125$ μm, and for $b_p/a = 0.136$. As shown in Table 3, most of the investigated crack arrest lengths were less than b_{p_tr}, which suggests that the uncoupled model was not appropriate, leading to dangerous underestimation of stress intensity factor values. The following analysis of the fretting crack arrest condition uses the complete coupled approach.

4.3. Definition of the crack path

4.3.1. Crack meshing

The crack propagation model is based on the elastic crack propagation mechanics strategy. A normal crack path description (Fig. 11a) is usually considered in the literature, as the stress intensity factor is based only on a mode I description. But, according to our results, the initial short crack is inclined with respect to the surface leading to a kinked sharped of the crack as

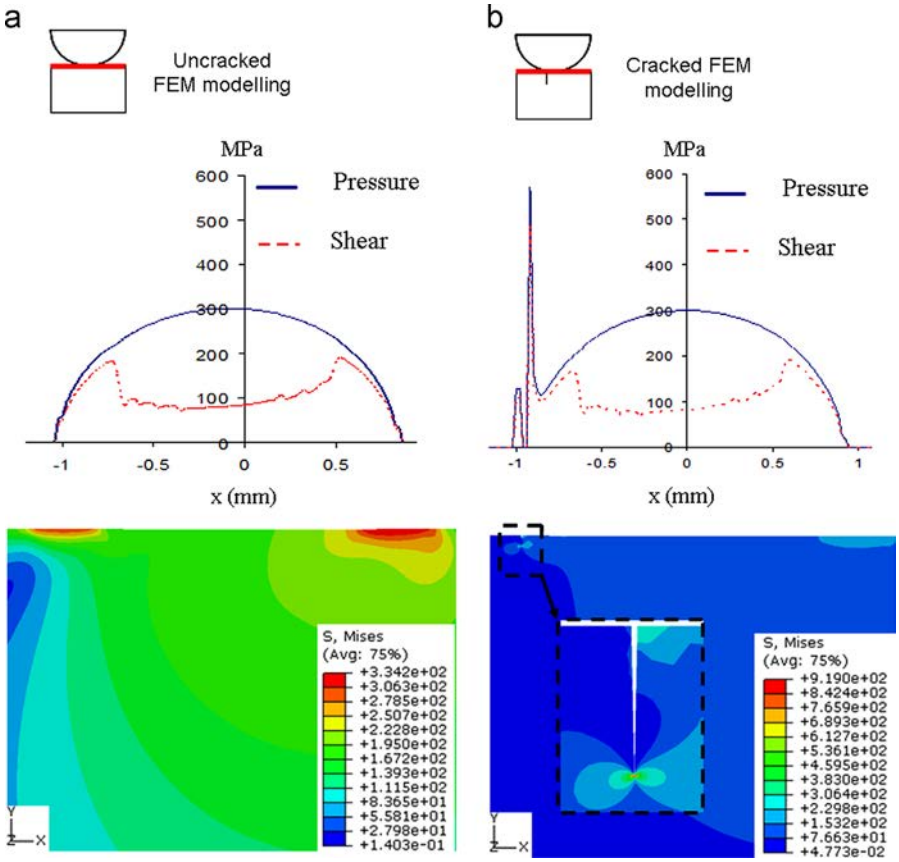

Fig. 10. Surface loadings and subsurface stress fields at $Q = +Q^*$ (q_{max} = 190 MPa, R = 80 mm) (a) Uncracked FEM modelling (decoupled approach) and (b) Cracked FEM modelling (coupled approach with b_p = 50 μm).

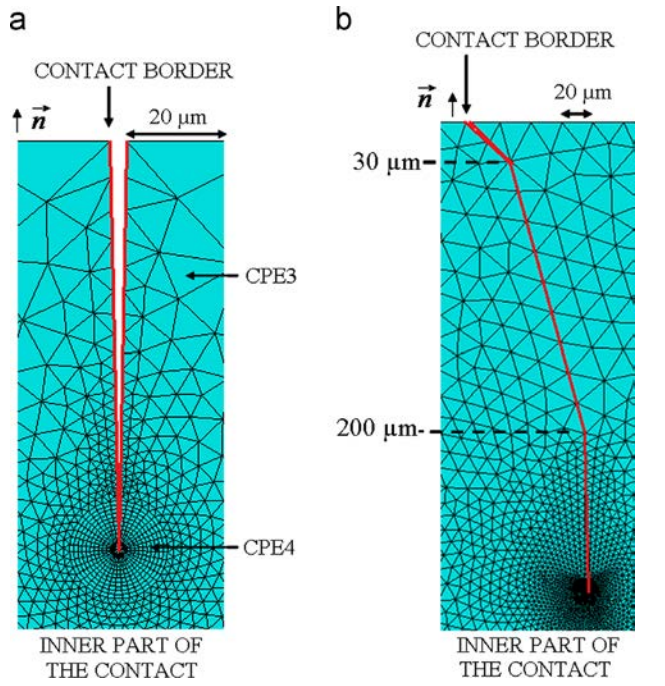

Fig. 11. Illustration of the two crack meshes used: (a) plain normal crack hypothesis and (b) kinked crack description.

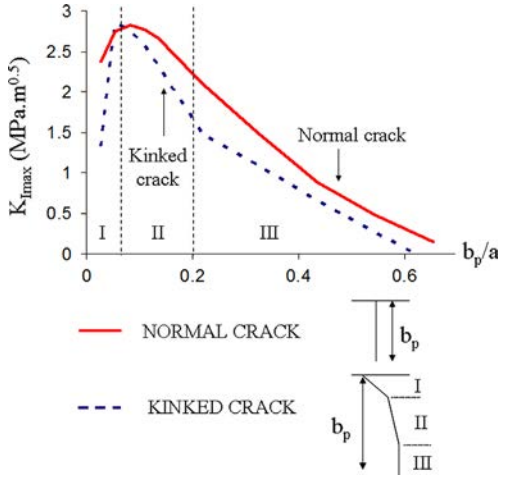

Fig. 12. K_{Imax} as a function of b_p/a ($q_{max}=190$ MPa, $R=80$ mm).

shown in Fig. 3. This part compares the contribution of the first (K_{Imax}) and second (ΔK_{II}) modes for two different crack paths: normal and kinked. This crack description is based on the experimental investigation (Fig. 11b). For both configurations, the crack was meshed at the contact border ($x=-a$) and the friction coefficient operating between the crack lips was considered in a first approximation as equivalent to the friction value at the partial slip transition (i.e., $\mu_{crack}=\mu_t=0.85$). Stress intensity factors were calculated using the Contour Integral method.

Fig. 12 focuses on K_{Imax} evolution. Considering the kinked crack description, three different zones were observed, corresponding to the three angles related to the crack path ($\Theta_1=47.5°$; $\Theta_2=15.5°$, $\Theta_3=0°$). The presence of an angle seemed to reduce the K_{Imax} value, so that the normal crack path description provided relevant conservative estimations. Note that both cracks were meshed at the contact border, just near the zone in compression induced by the contact normal loading. The stress intensity factor in mode I was directly bound to the projection of the stress field σ_{11}. In contrast to the normal crack, the kinked crack propagated into

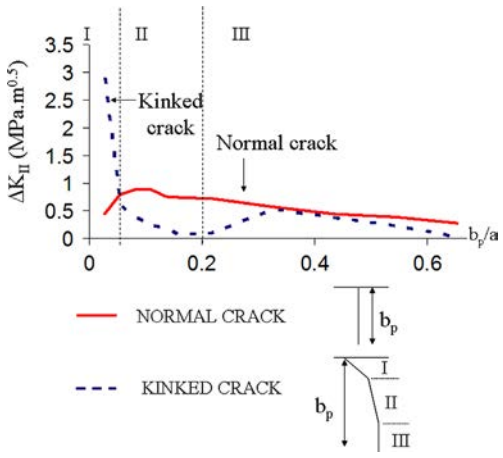

Fig. 13. ΔK_{II} as a function of b_p/a ($q_{max}=190$ MPa, $R=80$ mm).

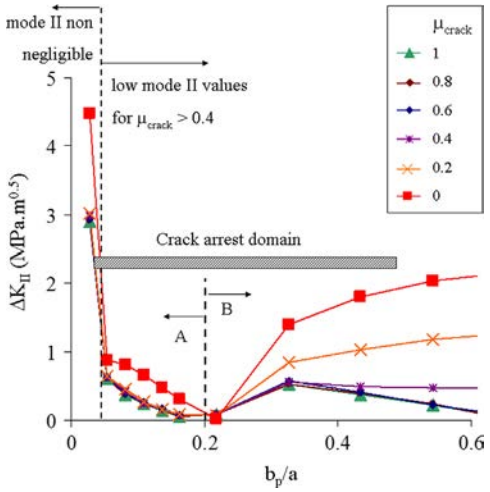

Fig. 14. Parametric study: ΔK_{II} as a function of b_p/a ($q_{max}=190$ MPa, $R=80$ mm).

the inner part of the contact, which was strongly affected by the compressive stress field induced by the normal loading. This tended to reduce the maximum value of K_{Imax} at the loading stage ($+Q^*$). A normal crack thus provided conservative values: K_{Imax} (Normal crack) > K_{Imax} (Kinked crack).

A second comparison concerned the evolution of the mode II stress intensity factor range (Fig. 13). It suggested that both normal and slant cracks models were equivalent for long cracks: $b_p/a > 0.2$. But for shorter cracks, especially for $b_p/a < 0.03$ (actually corresponding to the order of magnitude of the size of a grain), the kinked crack path had a non-negligible influence on the contribution of mode II: $\Delta K_{II\_KINKED} \gg \Delta K_{II\_NORMAL}$. This difference was due to the inclination of the crack with respect to the surface (45°) which results in a larger shear mode II contribution than in the normal description, generating shear more representative of reality. However, it can be concluded that a kinked crack description is much more relevant than the normal approximation to address the shear mode II contribution, which is predominant for the shortest cracks.

A kinked crack path description will be considered in the following, to describe short crack arrest processes.

4.3.2. *Influence of the friction value operating in the crack lips*

According to Fig. 13 which shows the mode II contribution of the kinked crack description, for very short cracks, due to the compressive state imposed during the unloading stage, the ΔK_{II} value is highly affected by the value of the friction coefficient μ_{crack}

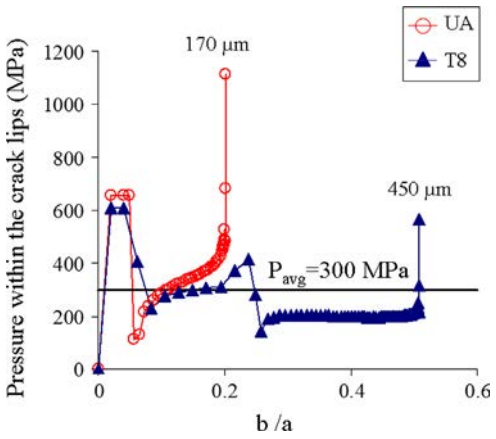

Fig. 15. Pressure profiles along the crack lips extracted from the FEM analysis related to the longest crack propagation condition (q_{max}=210 MPa, R=80 mm).

operating within the crack lips. To investigate this aspect, parametric analysis of ΔK_{II} evolution in a kinked crack was performed for various μ_{crack} values between 0 and 1 (Fig. 14). It revealed that, for very short cracks ($b_p/a < 0.05$), the mode II contribution had to be taken into account as it had non-negligible values compared to K_{Imax}. For longer cracks ($\mu_{crack} > 0.4$), on the other hand, mode II had a very small effect.

Analysis showed non-monotonic evolution. As expected, the ΔK_{II} contribution was significant for the initial short crack but sharply decreased to zero for $b_p/a \approx 0.2$ (domain A). In the deeper domain B ($b_p/a > 0.2$), the ΔK_{II} contribution showed an asymptotic increase which appeared highly dependent on the friction value.

A no-friction condition (μ_{crack}=0) led to significantly larger ΔK_{II} values in both domain A and B. ΔK_{II} evolution for larger μ_{crack} values then depended on the crack length domain. In the first domain A, it was surprising to see that all the curves were superimposed whatever the μ_{crack} value when $\mu_{crack} > 0.2$. This led to the important conclusion that, even if the friction value operating within the crack lips is not perfectly known, the ΔK_{II} estimation error will remain small.

For the deeper crack length $b_p/a > 0$ (domain B), a single master curve was observed where $\Delta K_{II} < 0.5$ MPa m$^{0.5}$ when $\mu_{crack} \geq 0.4$. The ΔK_{II} values obtained for μ_{crack}=0.2 were between the former lower bound and the higher bound related to the no friction condition.

Therefore, it can be concluded that, assuming $\mu_{crack} \geq 0.4$, all ΔK_{II} values are aligned along a single master curve (A&B) and the ΔK_{II} contribution is significant ($\Delta K_{II} \geq 0.5$ MPa m$^{0.5}$) only for the shortest crack domain ($b_p < 0.05$).

To estimate the μ_{crack} value, the following analysis was adopted:

First, the pressure profile operating along the crack path related to two longest crack arrest conditions of the two alloys was computed for the unloading compressive condition ($Q = -Q^*$). From this analysis, a mean pressure value P_{avg}=300 MPa could be extracted, representative of the maximum compression state generated in the crack lips during the fretting loading (Fig. 15).

To determine the corresponding friction values, a variable displacement analysis, equivalent to the fretting friction analysis, was performed. It consisted in plotting the evolution of the tangential force ratio $f = Q^*/P$ as function of the applied displacement, using homogenous 2196-T8/2196-T8 and 2196-UA/2196-UA flat/flat 4 mm × 4 mm square contact, applying a constant 300 MPa mean contact pressure (Fig. 16).

The tangential force ratio increased up to the transition between the partial and gross slip regimes, and then stabilized for large sliding amplitudes in the gross slip region. A constant gross slip friction value can be assumed: $\mu_{GS} = \mu_{crack}$=0.57 and will be considered in the following to describe the friction crack lip behaviour.

Note that the obtained μ_{crack} value of 0.57 was larger than the 0.4 threshold value discussed above. According to the parametric analysis described above, the ΔK_{II} contribution is found significant (≥ 0.5 MPa m$^{0.5}$) only for the very short cracks ($b_p/a < 0.05$). An error in μ_{crack} estimation is not significant for the ΔK_{II} value, as a single master curve is observed when $\mu_{crack} \geq 0.4$ (Fig. 14).

5. Results and discussion

5.1. Mixed mode analysis

For each b_{p_CA}, the corresponding K_{Imin}, K_{Imax}, K_{IImin} and K_{IImax} values were determined, considering the real crack path and friction within the crack lips (μ_{crack}=0.57).

To quantify the crack arrest condition, an effective value of the stress intensity factor range has to be approximated, such that:

$$\Delta K_{eff} = \sqrt{\Delta K_{eff\_I}{}^2 + \Delta K_{eff\_II}{}^2} \quad (6)$$

Regarding the mode II contribution, our FEM analysis considers the friction effect operating within the crack lips so it can be

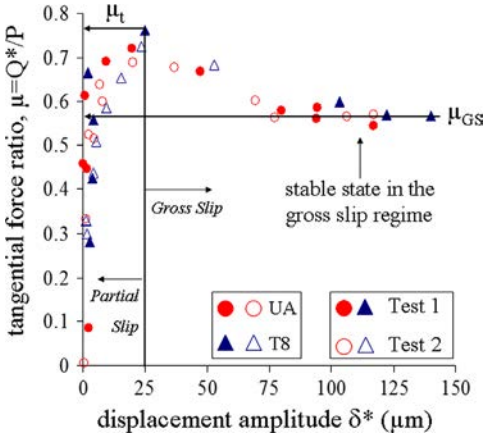

Fig. 16. Results of plane/plane variable displacement tests: evolution of the tangential force ratio as a function of sliding amplitude (P_{avg}=300 MPa).

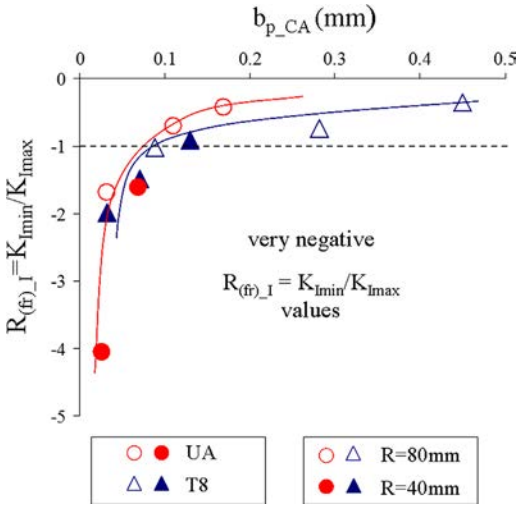

Fig. 17. $R_{(fr)\_I} = K_{Imin}/K_{Imax}$ for each crack arrest condition.

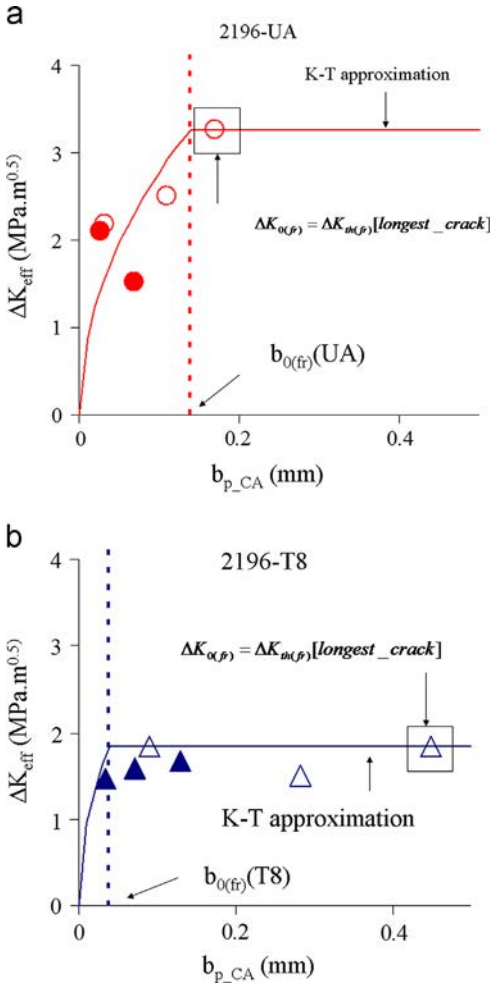

Fig. 18. ΔK_{eff} for each crack arrest condition related to K–T approximations – ●▲: R=40 mm – ○△: R=80 mm (a) 2196-UA and (b) 2196-T8.

assumed:

$$\Delta K_{eff\_II} = \Delta K_{II} = K_{II\_max} - K_{II\_min} \quad \text{with } \mu_{crack} = 0.57 \tag{7}$$

The ΔK_{eff_I} is more complex to address. Fig. 17 plots the evolution of the stress intensity factor loading ratio at the crack lips as a function of the projected crack length:

This shows that most of our fretting crack arrest conditions were observed for very negative $R_{(fr)}$ values, usually less than -1, except for the two longest cracks where the $R_{(fr)}$ ratio was between -1 and -0.4. Indeed the K_{Imin} and K_{Imax} values of the studied fretting configurations were respectively negative and positive (Table 3) corresponding respectively to the compression ($-Q^*$) and tensile ($+Q^*$) loadings. According to Elber's formalism, such very low $R_{(fr)}$ values suggest that K_{Imin} is negligible so that:

$$\Delta K_{eff\_I} = K_{Imax} \tag{8}$$

To conclude, the effective stress intensity factor range value is approximated by the following expression:

$$\Delta K_{eff} = \sqrt{K_{Imax}^2 + \Delta K_{II}^2} \tag{9}$$

Fig. 18 shows the $\Delta K_{eff}(b_{p\_CA})$ values related to the kinked FEM analysis of the experimental crack arrest conditions obtained for each UA and T8 heat treatments.

Asymptotic evolution can be characterised by a sharp increase of the threshold ΔK_{eff} for the short crack domain followed by a plateau evolution showing a constant $\Delta K_{th(fr)}$ response for the long crack domain. These typical evolutions are consistent with the short crack arrest description inspired by the Kitagawa-Takahashi formalism which was successfully adopted by Araujo et al. [1] for fretting fatigue analysis.

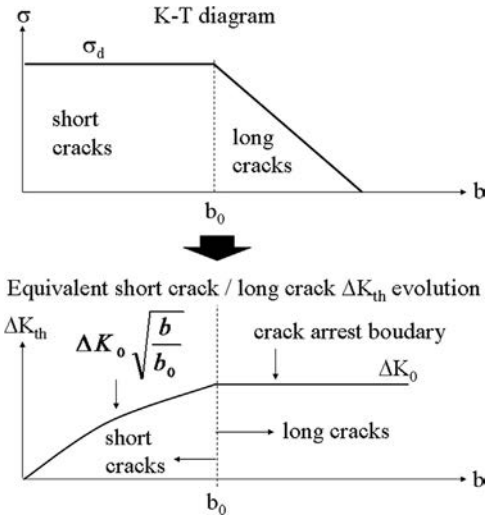

Fig. 19. Short crack/long crack formalism [3].

Indeed, as illustrated in Fig. 19, for the short crack arrest domain, $b < b_0$, the threshold crack arrest parameter was below the long crack threshold ΔK_0 but tended to increase with crack length, so that it could be taken as comparable to the K–T description provided by Nowell and other authors [1–3, 16]:

$$\Delta K_{th} = \Delta K_0 \sqrt{\frac{b}{b_0}} \quad \text{for } b < b_0 \tag{10}$$

For a long crack regime, ΔK_{th} is constant and equal to the maximal long crack threshold.

$$\Delta K_{th} = \Delta K_0 \quad \text{for } b > b_0 \tag{11}$$

The b_0 short crack/long crack transition is estimated from the following expression:

$$b_0 = \frac{1}{\pi}\left(\frac{\Delta K_0}{1.12\sigma_d}\right)^2 \tag{12}$$

However, to transpose this formalism it is necessary to know the fatigue limit (σ_d) and the long crack threshold value (ΔK_0). The fatigue limits are available (Table 2) but not the ΔK_0 values. To palliate such limitations, we assumed that longest crack lengths extracted from the plain fretting crack arrest analysis were governed by long crack behaviour. On this hypothesis, reverse analysis can be applied to extrapolate the threshold $\Delta K_{0(fr)}$ value from an adequate FEM model of the fretting crack arrest condition.

$$\Delta K_{0(fr)} = \Delta K_{eff(fr)}[\text{longest\_crack}] \tag{13}$$

For the two different heat treatments, this leads respectively to:

$\Delta K_{0(fr)}(\text{UA}) = 3.3 \text{ MPa } \sqrt{\text{m}}$

and

$\Delta K_{0(fr)}(\text{T8}) = 1.8 \text{ MPa } \sqrt{\text{m}}$.

Applying Eq. (12) to estimate the long crack transition leads respectively to:

$b_{0(fr)}(\text{UA}) = 137\ \mu m$

and

$b_{0(fr)}(\text{T8}) = 38\ \mu m$.

The corresponding ($\Delta K_{0(fr)}$, $b_{0(fr)}$) values were transposed in the K–T formalism (Eqs. (7) and (8)) and the evolution of ΔK_{th} compared to the experimental results (Fig. 18).

A very good correlation was observed for both the UA and the T8 heat treatments. The T8 treatment displayed a very rapid short/long crack transition, so most of the experiments operated in the long crack regime. This was confirmed by the plateau evolution, which indirectly supported the reverse fretting identification of the threshold ΔK_0.

In contrast, the UA treatment displayed a rather large short/long crack transition, so only the largest fretting crack was assumed to show long crack behaviour. This suggested that the given approximation of ΔK_0 was probably too conservative: plateau evolution was probably not complete, which implies that the true ΔK_0 value is probably larger than the present extrapolated $\Delta K_{0(fr)}$ value. Larger contact configurations inducing longer crack arrest situations need to be considered to achieve such plateau evolution and to provide a relevant approximation of ΔK_{th}, at least for material displaying a very slow long/short crack transition such as 2196-UA. However, the present model describes the short crack domain well (Fig. 18a, $b_p < b_0$), so the proposed approximation $\Delta K_{th(fr)}$ is probably not so far from the nominal value.

This analysis provides a quantitative comparison between the two alloys' crack arrest behaviours. The UA heat treatment led to a significant increase in crack arrest properties, improved by nearly 80% compared to T8 heat treatment: $\Delta K_{0(fr)}(UA)/\Delta K_{0(fr)}(T8) = 1.8$.

To validate this reverse fretting cracking analysis strategy, the obtained values could usefully be compared with classical CT fatigue experiments. Unfortunately, these data are not available. The comparison can only be addressed for the T8 heat treatment, with previous C-T results obtained on a similar 2196-T851 alloy for a 0.1 loading ratio [13]. The author found $\Delta K_{0(C-T)}$ (T851) = 2.9 MPa $\sqrt{m}$, which is of the same order of magnitude of the present value found from given fretting expertise: $\Delta K_{0(fr)}(T8) = 1.8$ MPa $\sqrt{m}$.

A major interest of this reverse plain fretting crack arrest analysis is the possibility of estimating the ΔK_0 value through a very fast and low-cost experimental investigation. Indeed, the plain fretting analysis requires a very small quantity of material, about few cm^3, compared to classical C.T. experiments, and this can be a decisive advantage for the development of new materials or the optimisation of new heat treatments.

5.2. Simplified approach: K_{Imax} approximation

The previous analysis was established considering the effective ΔK_{eff} value coupling mode I and II contributions. Integration of mode II is quite complex, because it requires estimating the friction μ_{crack} parameter and elaborate FEM simulations.

Our parametric analysis showed that, for $\mu_{crack} > 0.4$, the mode II contribution can be neglected ($b_p/a > 0.05$) in the whole crack arrest domain. Most metal interfaces display friction values larger than 0.4, implying that the present crack arrest analysis can be simplified, neglecting the shear mode II component, so that:

$$\Delta K_{eff} = K_{Imax} \tag{14}$$

Note that this approximation was previously exclusively applied in common plain fretting and fretting fatigue analysis [1,17]. The former analysis was therefore reinvestigated assuming a K_{Imax} approximation. Fig. 20 shows the corresponding K_{Imax} values related to the crack arrest condition as a function of the corresponding projected crack length. Again, asymptotic evolution from short crack to long crack plateau can be observed.

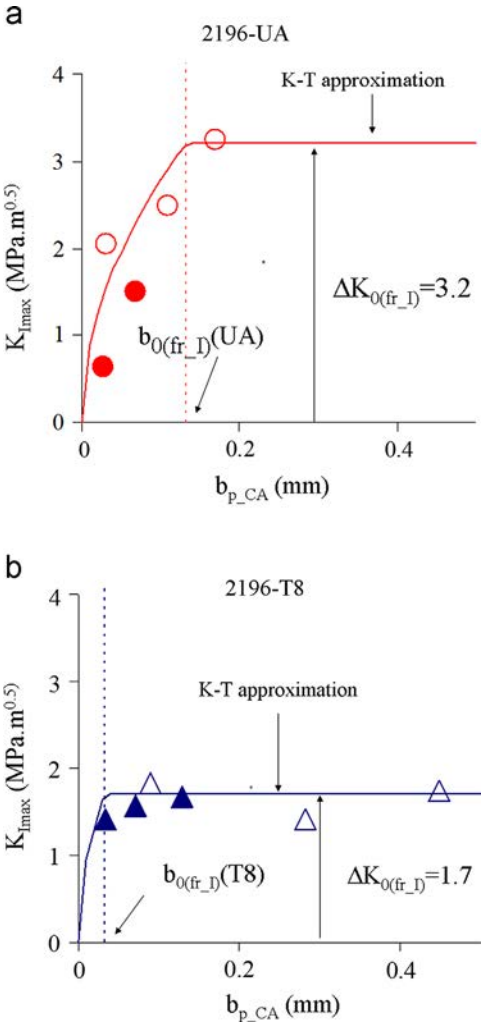

Fig. 20. Crack arrest using the K_{Imax} approximation – ●▲: R=40 mm – ○△: R=80 mm (a) 2196-UA and (b) 2196-T8.

ΔK_0 can be estimated by considering the longest crack arrest situations so that:

$$\Delta K_{0(fr\_I)} = \Delta K_{Imax}[\text{longest\_fretting\_crack}] \tag{15}$$

which leads respectively to:

$\Delta K_{0(fr\_I)}(UA) = 3.2$ MPa $\sqrt{m}$, $b_{0(fr\_I)}(UA) = 133\ \mu m$

and

$\Delta K_{0(fr\_I)}(T8) = 1.7$ MPa $\sqrt{m}$, $b_{0(fr\_I)}(T8) = 33\ \mu m$

The difference with respect to the complete mixed analysis is less than 5%. Again, a very good correlation can be observed with the K–T model, which confirms the stability of this approach, particularly for the T8 treatment where most of the results were in the plateau long crack response. Longer crack arrest conditions requiring larger contact dimensions are necessary to fully calibrate the UA treatment.

Hence it can be concluded that reverse identification of the short-to-long crack threshold crack arrest behaviour can be adequately quantified using a very basic K_{Imax} approximation, due to the very small influence of mode II in such plain fretting conditions.

6. Conclusion

An original methodology was developed to study the crack arrest condition by simple fretting experiments, and was applied to quantify the response of two different heat treatments, T8 and UA, performed on the same aluminium alloy 2196. The following points can be highlighted:

- The evolution of the stress intensity factor of fretting cracking was modelled using a coupled FEM approach which took into account the crack's effect on surface stress loading, crack path propagation in the plane, and the friction effect in the crack. This friction coefficient was estimated using tribologic fretting sliding analysis experiments: $\mu_{crack}=\mu_{GS}$.
- A reverse analysis was performed in order to establish the evolution of the crack arrest condition as a function of projected crack length ($\Delta K_{th(fr)}, b_{p\_CA}$).
- A methodology was established to estimate a crack arrest threshold by computing the stress intensity factor range related to the longest stopped fretting crack: $\Delta K_{0(fr)} = \Delta K_{eff}$[longest_fretting_crack].
- The evolution of computed $\Delta K_{th(fr)}$versus crack length was compared with the Kitagawa and Takahashi model. The correlation for the 2196-UA and –T8 alloys was very good. However it suggests that very large contact configuration involving longer crack arrest condition is needed when long/short crack transitions are identified.
- By this model it was possible to compare the properties of the two alloys quantitatively. The UA heat treatment induced an increase of about 80% in the crack arrest threshold ($\Delta K_{0(fr)}$).
- Initial comparison with results on conventional fatigue C-T samples (2196-T851) confirmed the present approach, but highlighted the necessity of performed classical CT fatigue experiments on the studied Al-alloys.
- The investigation shows that the mode II contribution is nearly negligible at least for metal crack interface where $\mu_{crack} > 0.4$. A basic K_{Imax} approximation can therefore be considered to formalize the crack arrest behaviour for the $\Delta K_{eff(fr)}$ estimation.

The present method of identifying crack arrest threshold on simple fretting tests is of demonstrated interest, allowing crack arrest conditions to be studied over a wide spectrum of crack lengths simply by changing the contact dimension: i.e., by changing the cylinder radius.

Furthermore, this analysis can be performed on very small volumes of materials, which may present a certain technical and economic interest.

Finally, it is possible to study the influence of surface heat treatment more finely, in terms of crack arrest threshold.

Acknowledgements

The authors want to thank the Carnot Institute (I@L) for partial financial support of this research and the Constellium CRV company (A. Danielou) for supplying material specimens.

References

[1] Araújo JA, Nowell D. Analysis of pad size effects in fretting fatigue using short crack arrest methodology. Int J Fatigue 1999;21:947–56.

[2] Fouvry S, Kubiak K. Development of a fretting–fatigue mapping concept: the effect of material properties and surface treatments. Wear 2009;267:2186–99.

[3] Dini D, Nowell D, Dyson. IN. The use of notch and short crack approaches to fretting fatigue threshold prediction: theory and experimental validation. Tribol Int 2006;39:1158–65.

[4] Delacroix J. Etude des Mécanismes de Fissuration en Fatigue et/ou Fretting d'Alliages Al–Cu–Li [Ph.D. thesis]. Institut National des Sciences Appliquées de Lyon 2011. ⟨http://theses-search.insa-lyon.fr/thematic-search.html?menuKey=theses_insa&submenuKey=authors&id=delacroix_jessica⟩ [accessed September 2013] [in French].

[5] Heredia S, Fouvry S. Introduction of a new sliding regime criterion to quantify partial, mixed and gross slip fretting regimes: correlation with wear and cracking processes. Wear 2010;269(7–8):515–24.

[6] Fouvry S, Gallien H, Berthel B. From uni- to multi-axial fretting-fatigue crack prediction: development of a stress-gradient-dependent critical distance approach. IJF. http://dx.doi.org/10.1016/j.ijfatigue.2013.05.016.

[7] Bueckner HF. A novel principle for the computation of stress intensity factors. Z Angew Math Mech 1970;50:529–46.

[8] Rice JR. A path independent integral and the approximate analysis of strain concentration by notches and cracks. J Appl Mech 1968;35:379–86.

[9] Dolbow J. An extended finite element method with discontinuous enrichment for applied mechanics [Ph.D. thesis]. Northwestern University; 1999.

[10] Yau J, Wang S, Corten H. A mixed-mode crack analysis of isotropic solids using conservation laws of elasticity. J Appl Mech 1980;47:335–41.

[11] Shih C, Asaro R. Elastic-plastic analysis of cracks on bimaterial interfaces: part I—small scale yielding. J Appl Mech 1988;55:299–316.

[12] Giner E, Tur M, Vercher A, Fuenmayor FJ. Numerical modelling of crack-contact interaction in 2D incomplete fretting contacts using X-FEM. Tribol Int 2009;49(9):1269–75.

[13] Richard S. Fissuration par fatigue d'alliages d'aluminium au lithium de troisième génération [Ph.D. thesis]. Mecanique, Energetique et Aeronautique: Sciences et Ingenierie en Materiaux; 2011.

[14] Proudhon H, Basseville S. Finite element analysis of fretting crack propagation. Eng Fract Mech 2011;78:685–94.

[15] Proudhon H, Fouvry S, Buffiere JY. Characterisation of fretting fatigue damage using synchrotron X-ray micro-tomography. Tribol Int 2006;39:1106–13.

[16] Fouvry S, Nowell D, Kubiak K, Hills DA. Prediction of fretting crack propagation based on a short crack methodology. Eng Fract Mech 2008;75(6):1605–22.

[17] Delacroix J, Cazottes S, Daniélou A, Fouvry S, Buffière JY. Influence of microstructure on the fretting resistance of Al–Cu–Li alloys. In: Proceedings of the ICAA13 13th international conference on aluminium alloys; 2012.